JOURNAL OF AIRCRAFT
Vol. 42, No. 2, March–April 2005

Computations with *k–g* Model for Complex Configurations at High-Incidence

Zhixiang Xiao,* Haixin Chen,† and Song Fu‡
Tsinghua University, 100084 Beijing, People's Republic of China
and
Fengwei Li§
Northwestern Polytechnical University, 710072 Xi'an, People's Republic of China

The two-equation *k–g* turbulence model, a derivation of the *k–ω* model, with its advantages such as no use of normal-to-wall distance, simple source terms, and straightforward boundary conditions, can be easily applied in complex computational fluid dynamics applications. Transonic flows around the ONERA M6 wing and the NASA TN D-712 wing–fuselage model at angles of attack of 12.5 and 26.2 deg are first used to validate the codes. Then the transonic flows around an F-22-like complete aircraft configuration are numerically simulated at angles of attack from 0 to 48 deg. The computational results are compared to available experimental data, and good agreement is achieved. The results of the algebraic Baldwin–Lomax model is also presented for comparison.

I. Introduction

COMPUTATIONAL fluid dynamics (CFD) methods have been widely used in the design of aircraft. Because of the great difficulties in experimental study, CFD demonstrates its great importance in the simulation of transonic high-angle-of-attack (AOA) flow about realistic configurations, which is dominated by extremely complex phenomena such as shock/boundary-layer interaction, massive flow separation, and complicated vortex structures. Until now, numerical prediction of such phenomena has been highly dependent on the selection of turbulence models.

Two-equation models are commonly thought more appropriate for modeling of complex flow, when compared to algebraic model, because they require less empiricism, incorporate substantially more physics, and, therefore, can take into account history effects.[1] When Boussinesq approximation is used, the number of necessary transport equations is much less than that of more complex models, such as second-moment closure models. Their computation costs and numerical properties are, hence, comparatively more acceptable.

In three-dimensional simulation about realistic configurations, multiblock grid technology is usually employed. Because of the geometry complexity, there are often intersections between wall surfaces, such as wing–fuselage junctions, fin–tail–plane junctions, etc. These intersections make it ambiguous to define an appropriate wall distance for grid cells. The application of wall functions also becomes very complicated. On the other hand, for high-AOA flow, the rationality of the wall function often becomes questionable because of the massive separation. Therefore, the low Reynolds number models without use of wall distance are preferred for the CFD research in aircraft design.

The Wilcox[2] k–ω is such a model. However, its wall boundary conditions for the ω equation are unsatisfactory and prevent it from convenient application. By its definition, ω needs to be infinity at the wall. Such a boundary condition is hard to realize and will cause stiffness and stability problems in the numerical process. Another well-known shortcoming of Wilcox k–ω model, as pointed out by Menter,[3] is that the Reynolds stress predicted is greatly dependent on the specified freestream value of ω.

To overcome the shortcomings, Menter developed baseline (BSL) k–ω and shear stress transport (SST) k–ω models. Unfortunately, both models introduced the wall distance. Kalitzin et al.[4] reformulated the ω equation and derived the k–g model. This model preserves the advantages of the k–ω model: both its low Reynolds number characteristics and the absence of wall distance in the formulation. At the same time, this model has straightforward boundary conditions, and its source terms show better numerical properties. In Ref. 4, the accuracy and efficiency of the k–g model are demonstrated by applications ranging from airfoil to regional jet transport.

In this paper, the results for ONERA M6 wing are presented to demonstrate the improvement of the k–g model vs the k–ω model. The NASA TN D-712 standard wing–fuselage model,[5] for which detailed high-AOA experimental data are available, is also calculated to validate the capability and accuracy of the k–g model and its solution methods. Then the high-AOA transonic flows about an F-22-like complete fighter configuration[6] composed of fuselage, wing, strake, cockpit, horizontal tail, outward oblique vertical tail, and ventral fin is simulated. The results of Baldwin–Lomax[7] model are also presented for comparison.

II. Turbulence Models

A. *k–g* Model

As a two-equation eddy viscosity model, two transport equations in addition to the Reynolds averaged Navier–Stokes (RANS) equations need to be solved. As a widely accepted choice, the equation for turbulent kinetic energy,

$$\frac{\partial(\rho u_i k)}{\partial x_i} = \frac{\partial}{\partial x_i}\left[\left(\mu_l + \frac{\mu_t}{\sigma_k}\right)\frac{\partial k}{\partial x_i}\right] + P_k - \rho\varepsilon \qquad (1)$$

is used as the first equation. Here P_k is the production of k, and ε is the specific turbulence dissipation rate.

The other equation should be formulated to achieve the closure of the system. Besides the k–ε class models, which give a transport equation for ε directly, the k–ω model developed by Wilcox[2] can be written as

$$\frac{\partial(\rho u_i k)}{\partial x_i} = \frac{\partial}{\partial x_i}\left[\left(\mu_l + \frac{\mu_t}{\sigma_k}\right)\frac{\partial k}{\partial x_i}\right] + P_k - \beta^*\rho k\omega \qquad (2)$$

Received 3 December 2003; presented as Paper 2004-0899 at the AIAA 42nd Aerospace Sciences Meeting and Exhibit, Reno, NV, 5–8 January 2004; revision received 10 February 2004; accepted for publication 11 February 2004.

*Postdoctoral Researcher, Department of Engineering Mechanics.
†Lecturer, Department of Engineering Mechanics.
‡Professor, Department of Engineering Mechanics. Member AIAA.
§Professor, College of Aeronautics, Shaanxi Province. Member AIAA.

$$\frac{\partial(\rho u_i \omega)}{\partial x_i} = \frac{\partial}{\partial x_i}\left[\left(\mu_l + \frac{\mu_t}{\sigma_\omega}\right)\frac{\partial \omega}{\partial x_i}\right] + \alpha\frac{\omega}{k}P_k - \beta\rho\omega^2 \quad (3)$$

where ω is defined as $\varepsilon/(k\beta^*)$.

Equation (3) can be integrated to the wall without the damping functions; hence, the model is thought as a low Reynolds number model. Furthermore, no normal-to-wall distance is presented in the formulation. However, the boundary condition for ω is very challenging. Because $\omega \propto \varepsilon/k$ and k is zero at the solid surface, the ω will approach infinity at the wall. Wilcox[8] and Menter[9] suggested functions specifying large enough values of ω on the one or several grid cells next to the wall according to their distance from the wall. It is obvious that the effect of these treatments heavily rely on the near-wall grid spacing. In CFD application, an abruptly large value set on the boundary often makes convergence very hard to be achieved.

To avoid the boundary condition problems, Kalitzin et al.[4] reformulated the ω equation Eq. (3) and expressed them as the term $g = (\beta^*\omega)^{-1/2}$. The square of the variable g has the units of time. It goes to zero at a solid surface.

To eliminate the results' dependence on the freestream quantities and suppress the high levels of g outside of the boundary,[4] the source terms are modified by introducing a limiter based on local eddy viscosity, $R = \max(0.01\mu_l, \mu_t)$.

The new model is given as

$$\frac{\partial(\rho u_i k)}{\partial x_i} = \frac{\partial}{\partial x_i}\left[\left(\mu_l + \frac{\mu_t}{\sigma_k}\right)\frac{\partial k}{\partial x_i}\right] + P_k - \frac{\beta^*\rho^2 k^2}{R} \quad (4)$$

$$\frac{\partial(\rho u_i g)}{\partial x_i} = \frac{\partial}{\partial x_i}\left[\left(\mu_l + \frac{\mu_t}{\sigma_g}\right)\frac{\partial g}{\partial x_i}\right] - \alpha\frac{\beta^*\rho g^3}{2R}P_k + \frac{\beta\rho^2 k g}{2R} - \left(\mu_l + \frac{\mu_t}{\sigma_g}\right)\frac{3\beta^*\rho k g}{R}\frac{\partial g}{\partial x_i}\frac{\partial g}{\partial x_i} \quad (5)$$

The eddy viscosity is $\mu_t = \beta^*\rho k g^2$, and the constants are $\sigma_\kappa \equiv \sigma_\omega \equiv \sigma_g = 2$, $\alpha = \frac{5}{9}$, $\beta^* = 0.09$, and $\beta = 0.075$.

The boundary treatment becomes rational and simple. The turbulent kinetic energy k and the variable g are both set to zero at the wall. At the inflow boundaries, the turbulent quantities are specified, and at outflow boundaries, a zero gradient is assigned.

B. Baldwin–Lomax Model

The Balwin–Lomax (B–L) turbulence model[7] is widely used in CFD research; its capability and limitation are both well known. For attached flow and flow with small separation, it can get fairly good results.

B–L model is an algebraic model based on the mixing-length assumption. The inner eddy viscosity is given as

$$\mu_{t,i} = \rho(0.4D\eta)^2\Omega \quad (6)$$

where $D = 1 - \exp(-\eta^+/26)$, $\eta^+ = \eta(\rho_w\tau_w)^{0.5}/\mu_w$, ρ is the density, η is the distance to the wall, Ω is the magnitude of vorticity, and the subscript w refers to a wall value.

The outer eddy viscosity is determined via

$$\mu_{t,0} = (0.0168)(1.6)\rho F_{\text{wake}}\Gamma \quad (7)$$

where $F_{\text{wake}} = \text{minimum}\{0.25\eta_{\max}(q_{\max} - q_{\min})^2/F_{\max},\ \eta_{\max}F_{\max}\}$, $\Gamma = 1/[1 + 5.5(0.3\eta/\eta_{\max})^6]$, $F(\eta) = \eta\Omega D$, $F_{\max}$ is the maximum value of $F(\eta)$ that occurs in a profile, and $\eta_{\max}$ is the value at which $F_{\max}$ occurs. The symbol q denotes the modular of velocity.

Here, the inner and outer models are blended to obtain the eddy viscosity using the similar function as the Johnson–King[10] model,

$$\mu_t = \mu_{t,0}[1 - \exp(-\mu_{t,i}/\mu_{t,0})] \quad (8)$$

This modification has been proven to be able to improve the robustness and convergence.

III. Numerical Methods

The computations in this paper are all based on a three-dimensional multiblock compressible RANS solver with a Jamesontype cell-centered finite volume formulation and a modified four-step Runge–Kutta explicit time stepping. Artificial dissipation with blended second- and fourth-order difference is used for shock wave capture and unphysical oscillation suppression. Local time stepping and implicit residual smoothing are employed to accelerate the convergence.

To enhance the robustness of artificial dissipation, the original scheme[11] is modified according to Ref. 12 in this paper. The anisotropic artificial dissipation is applied to reduce the disturbance of artificial dissipation to the physical viscosity. To improve the accuracy of the shock capture and increase the stability of scheme, the shock sensor is modified as[13]

$$\psi_i = \frac{|P_{i-1} - 2P_i + P_{i+1}|}{\phi(P_{i-1} + 2P_i + P_{i+1}) + (1-\phi)(|P_i - P_{i-1}| + |P_{i+1} - P_i|)} \quad (9)$$

where P_i is the static pressure and $0 < \phi \leq 1$. Such a modified artificial dissipation has a total variation diminishing property. When $\phi = 1$, it returns to the original Jameson et al. expression in Ref. 11. We set $\phi = 0.5$ in this paper.

At far-field boundaries, the one-dimensional Riemann characteristic analysis is employed to construct a nonreflection boundary condition. For smooth surfaces, no-slip boundary conditions are used.

For most two-equation turbulence models, because the turbulence transport equations include important source terms, the system becomes numerically very stiff, and they often need to be solved with strong implicit methods. However, for the k–g model, according to our experience, the turbulence equations can be explicitly solved with the same spatial and time scheme as the mean flow equations. The system can be kept stable through the use of smaller Courant–Friedrichs–Lewy number and careful selection of the artificial dissipation coefficients.

The solutions of the turbulence transport equations are decoupled from the mean flow solution. Artificial dissipation and implicit residual smoothing are also constructed for the k and g equations in a similar manner.

IV. Results and Discussion

In this paper, for an aircraft configuration, the coordinate system is set as follows: x is the streamwise direction, and z is the spanwise direction. B denotes the full span. $B/2$ is chosen as the character length for all of the cases.

The grids are created by solving elliptic equations. Appropriate zonal decomposition and grid topology selection are performed according to the characteristics of the configuration.

A. ONERA M6 Wing

The ONERA M6 wing is a widely used three-dimensional test case for the validation of numerical methods and turbulent models. The flowfield is computed here at a freestream Mach number of 0.84 and an AOA of 6.06 deg. The freestream Reynolds number is 11.7×10^6.

The pressure coefficients results are compared on the wing sections located at 44, 65, 80, and 90% half-span. Results in Ref. 14 computed by k–ω are also shown in Fig. 1 compared to the present results by the k–g model. Although the k–g model is derived from the k–ω model, there are some differences between their results, mainly because of the limiters in the formulation. From Fig. 1, it is observed that the shock position of the k–g results is located upstream to that of the k–ω results, especially at the wing tip.

B. NASA TN D-712

This wing–body configuration consists of a lower aspect ratio midwing with large swept angle and a fuselage with pointed nose. O–H-type grids are used in the region of wing and aft body. To avoid

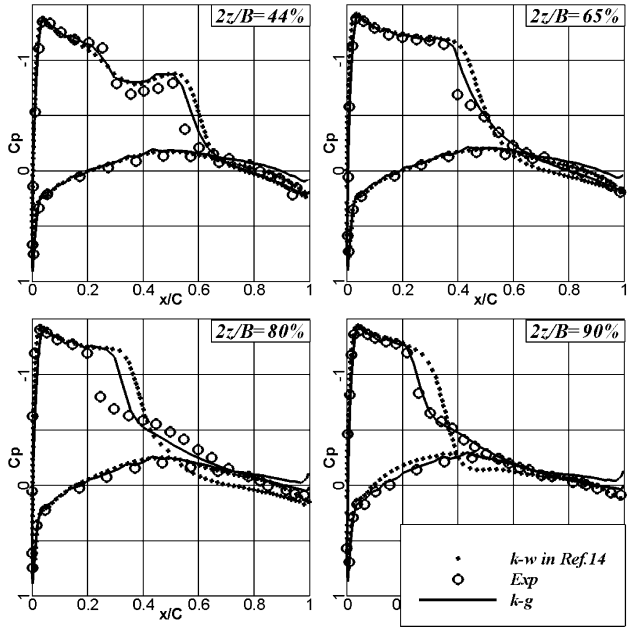

Fig. 1 Surface pressure coefficients on the wing.

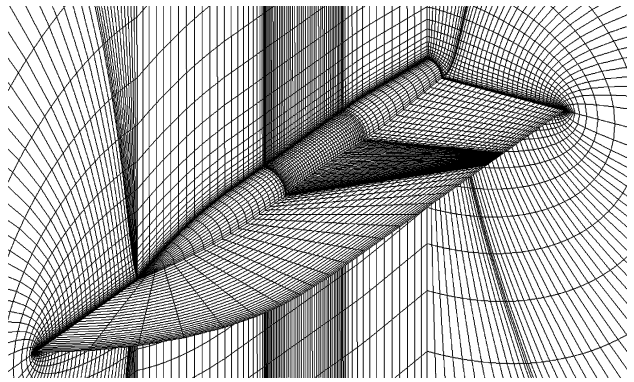

Fig. 2 Space and surface grids around TN D-712.

a singularity mesh line from the nose to the far field,[15] the topology is shifted to O–O type near the forebody. There are $95 \times 79 \times 45$ grid points (streamwise/circumferential/normal) used. The grids are shown in Fig. 2. The minimum normalized grid spacing to the wall is 2.5×10^{-5}. The radius of the far-field grid boundaries surface is 12.5.

The computations are performed for the Mach number 0.9 cases. The Reynolds number is 7.5×10^6. Results of two AOA are presented. One is 12.5 deg and the other 26.2 deg. In both cases, the flows are separated with vortices emerging from the wing leading edge or even the forebody.

Case 1: AOA = 12.5 Degrees

Figure 3a (AOA = 12.5 deg case) shows the comparison of surface pressure coefficients among the results of B–L model, k–g model, and experimental data. Results on six wing spanwise locations are presented. Very serious aerodynamics interference between the wing and fuselage can be found on the pressure distribution of wing root sections at $2z/B = 16\%$ and 25%, where k–g model's results match the experimental results much better than those of B–L model. The lack of history effects makes B–L model unable to predict the interaction very well. At $2z/B > 60\%$, the flow is completely separated, and the pressure coefficients on the upper surface almost look like a straight line. Although the results of k–g model match the experiment well there, little disturbance at the leading edge can be observed at the $2z/B = 95\%$ section. The B–L model's results deviate badly from that of the k–g model

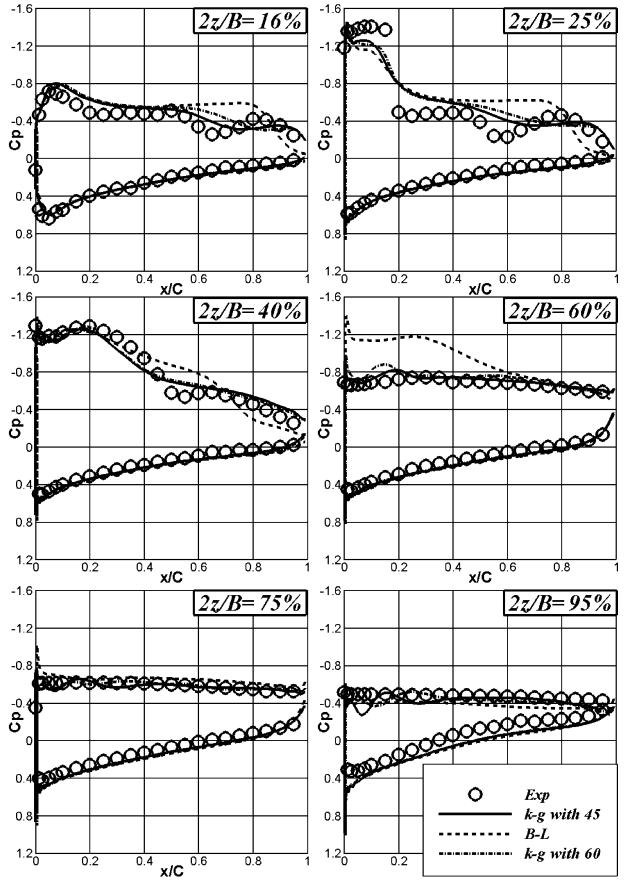

Fig. 3a Surface pressure coefficients on the wing, AOA = 12.5 deg.

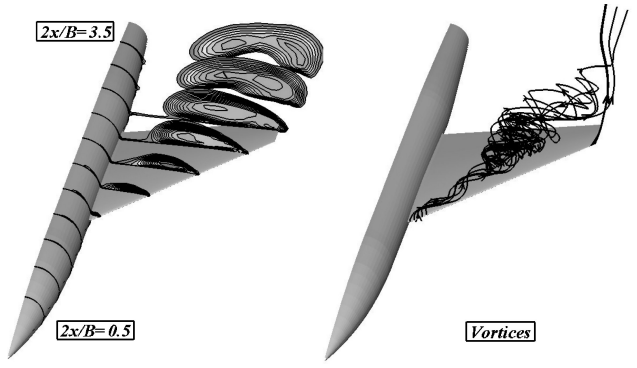

Fig. 3b Vortices over the wing–body, AOA = 12.5 deg.

results and experimental data at $2z/B = 60\%$; this indicates that the spanwise range of the outer wing separation is under predicted by it.

Some results by k–g model with 60 normal grids are also plotted in Fig. 3a. Little difference can be observed between the dense and coarser grids.

The vortices structure predicted with k–g model are shown in Fig. 3b. At this relatively lower AOA, the vortex from the forward fuselage is much weaker than that from the leading edge of the wing.

Case 2: AOA = 26.2 Degrees

At higher alpha, the flow over the upper surface of the TN D-712 is almost entirely separated. The vortices from the forebody and the wing leading edge are much stronger than those in case 1, as shown in Fig. 4a (AOA = 26.2 deg). The vortices detached from the forebody are merged into the wing leading-edge vortices, by which the separation of the whole upper wing is induced.

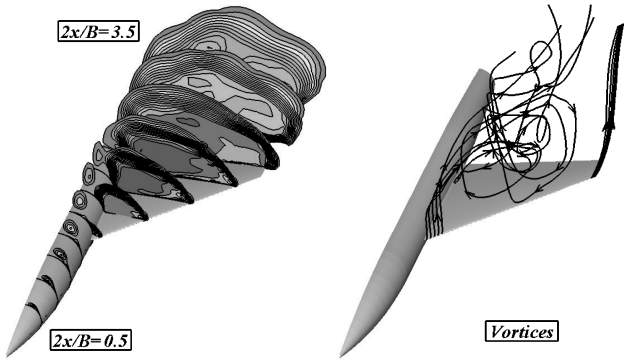

Fig. 4a Vortices over the TN D-712, AOA = 26.2 deg.

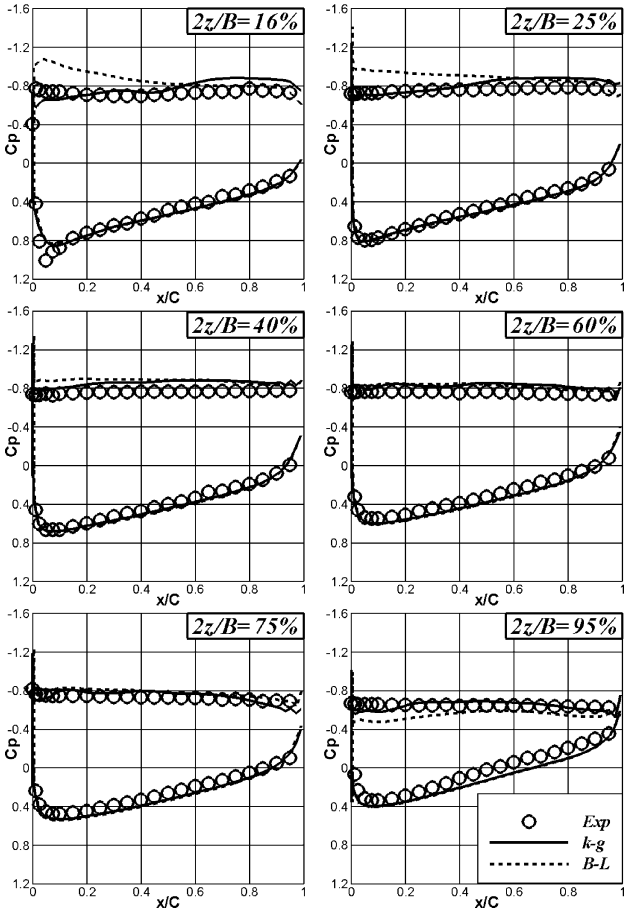

Fig. 4b Surface pressure coefficients on the wing, AOA = 26.2 deg.

The results of surface pressure coefficients are shown in Fig. 4b. Again, the k–g model shows better results than those of the B–L model, especially at sections near the root. Near the wing tip, the results over the upper surface of the B–L model show some mismatch to experimental data.

C. F-22-Like Complete Aircraft Model

Three grid blocks are used to model the extremely complex configuration. The grid numbers are $110 \times 21 \times 52$, $110 \times 63 \times 52$, and $110 \times 15 \times 52$. The grid blocks are point-to-point patched to each other. Because of the complexity of this configuration, the minimum grids spacing, about 5×10^{-5}, is larger than that of the TN D-712. The normalized far-field boundaries radius is still 12.5. Figure 5 shows the surface and space grids around this complete aircraft. The grids of some typical sections are also shown in Fig. 5.

Several transonic cases are calculated with the AOA ranging from 0 to 48 deg. The Mach number is 0.8, and the Reynolds number

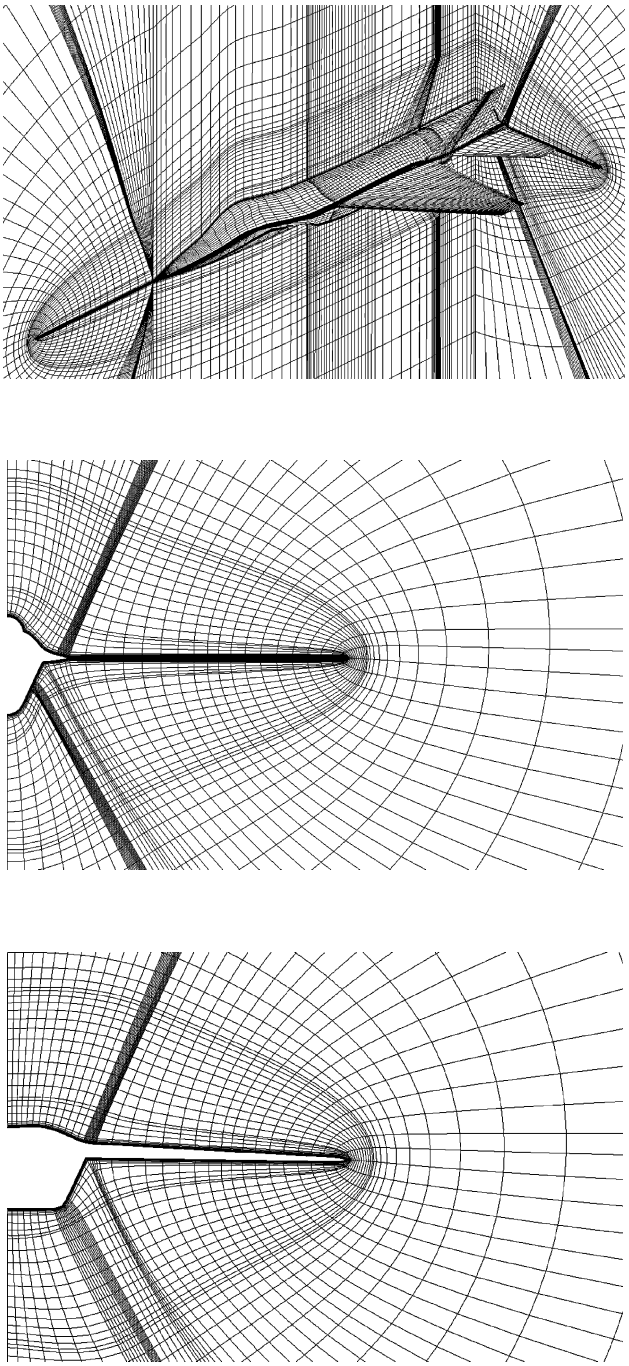

Fig. 5 Space grids with three blocks around the complete aircraft.

is 5×10^6. The experimental data of surface pressure coefficients over the wing are not available. Only the lift and pitching moment data are compared with computational results in Fig. 6. Although the experimental data of drag are not available, the computational results are also plotted. The lift and drag coefficients predicted with the B–L and k-g models show little difference. They match the experimental data very well at AOAs under 24 deg. At higher AOA, the absolute values of lift and drag of the B–L model are a little bit lower than those of the k–g model. The pitching moment coefficient shows more sensitivity to the models. The k–g model shows quite good agreement throughout the experimental AOA range, Whereas the B–L model underpredicts the pitching moment.

The convergence history of C_l and C_d are plotted in Fig. 7.

To understand the flow structure and characteristics, computational results of some typical cases are described in the following subsections.

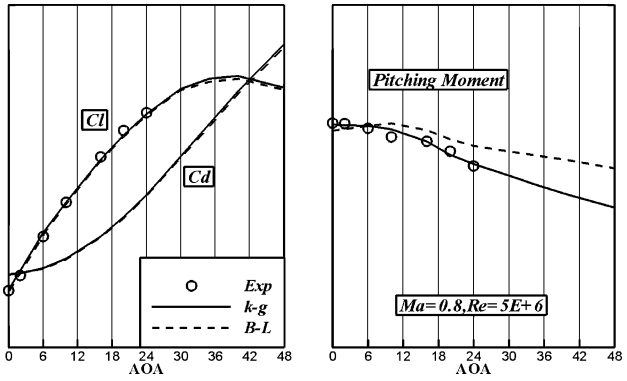

Fig. 6 Comparisons of lift, drag, and pitching moment.

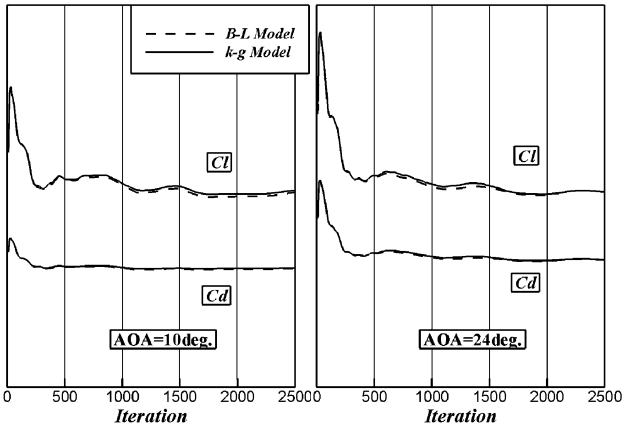

Fig. 7 History of lift and drag.

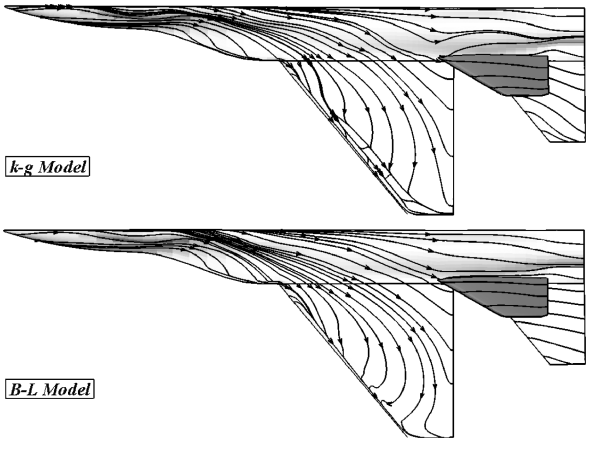

Fig. 8a Streamlines on the upper surface, AOA = 10 deg.

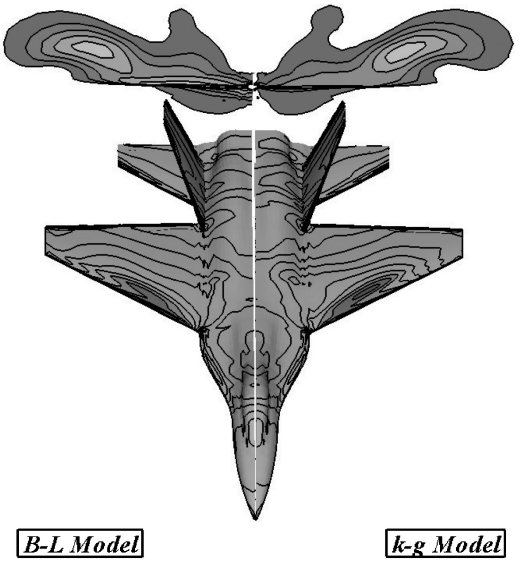

Fig. 8b Components effect on the wake, AOA = 10 deg.

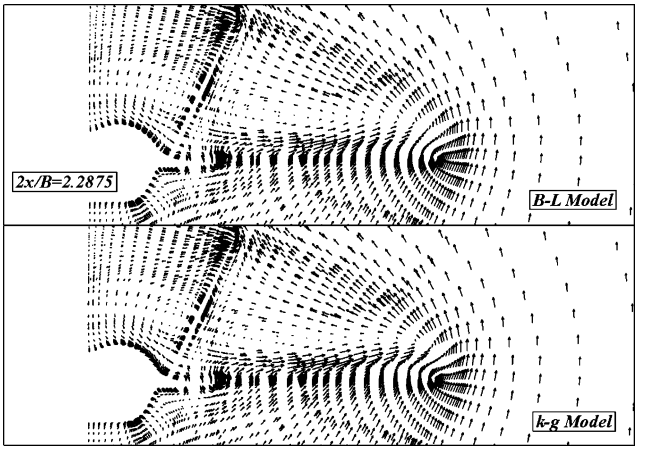

Fig. 8c Velocity vectors at $2x/B = 2.2875$, AOA = 10 deg.

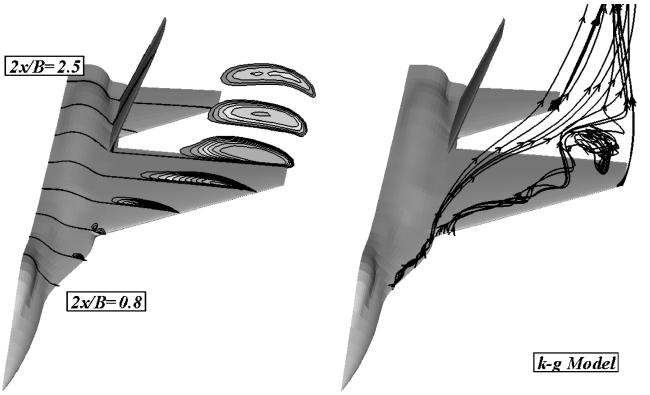

Fig. 8d Vortices over the wing with k–g model, AOA = 10 deg.

Case 1: AOA = 10 Degrees

As shown in Fig. 8a (AOA = 10 deg) the distinct difference between the two models is that the k–g predicted secondary separation area on the leading edge is larger than that of the B–L model.

The effects of the fin, tail, and the aft fuselage on the wake can be analyzed in Fig. 8b. The difference between the B–L and k–g models can be found in the total pressure distribution over the upper surface, especially on the wing.

The velocity vectors projected on the y–z surface at the axial location $2x/B = 2.2875$ are plotted in Fig. 8c. The station is just located at the leading edge of the vertical tail tip. Figure 8d shows the space vortices structure predicted by the k–g model. Two vortex cores can be observed on the wing apex section. One is rolled up from the strake, the other is from the wing apex. The two vortices move outward and, therefore, do not collide with the vertical tail. A separation bubble formed by the vortex from the wing apex is also observed above the wing tip.

Case 2: AOA = 24 Degrees

At a higher AOA the separation over the upper surface is more serious. In the k–g results, the strake vortex merges into the wing vortex at the section $2x/B \approx 1.5$, as shown in Fig. 9a (AOA = 24 deg). The vertical tail is almost submerged in the vortices.

Figure 9b shows the total pressure contour on the upper surface and in the wake computed by the two models. The low total pressure regions at the apex of strake, wing, and horizontal stabilizer are very distinct.

The surface pressure coefficients over the wing are shown in Fig. 9c. The difference between the two models is very small. Because of the wing–body amalgamation design, the advantage of the k–g model in the prediction of wing–body interference, which has been thoroughly revealed in the case of TN D-712, does not appear here.

The separation shown in Fig. 9d is so severe that the vortex cores move upward more than in case 1.

Figure 9e shows the case's convergence history of the maximum and mean residuals in different grid blocks. Because of the unsteady

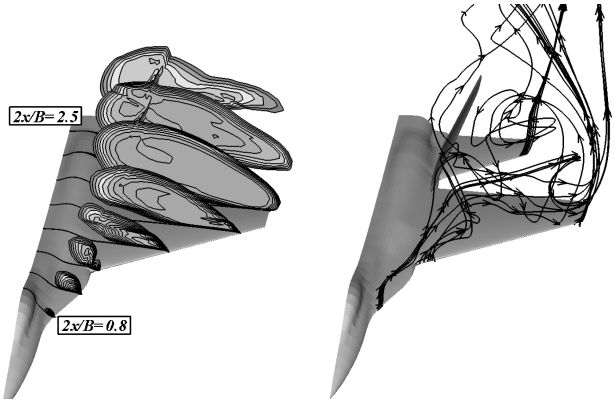

Fig. 9a Vortices over the wing, AOA = 24 deg.

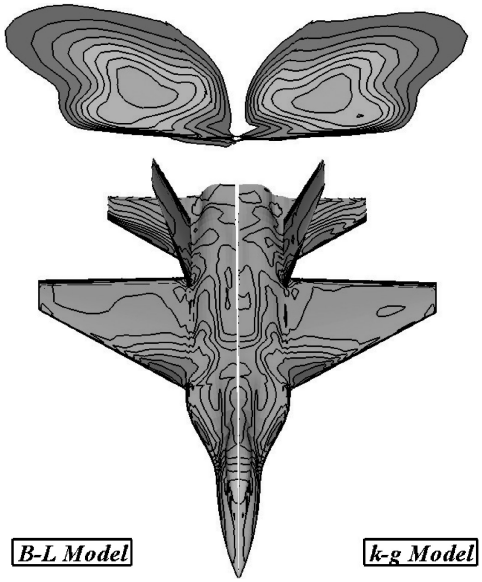

Fig. 9b Total pressure contour on the surface and in wake, AOA = 24 deg.

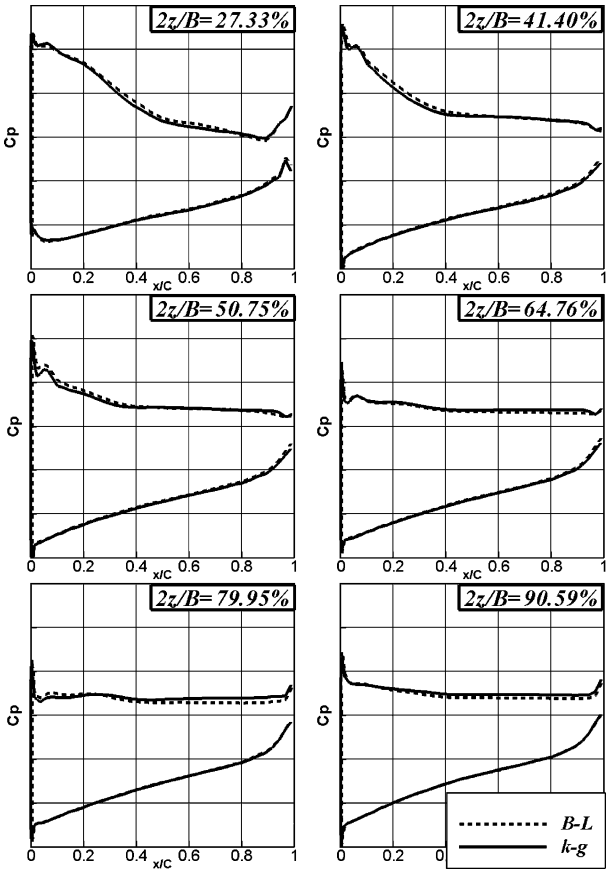

Fig. 9c Surface pressure coefficients over the wing, AOA = 24 deg.

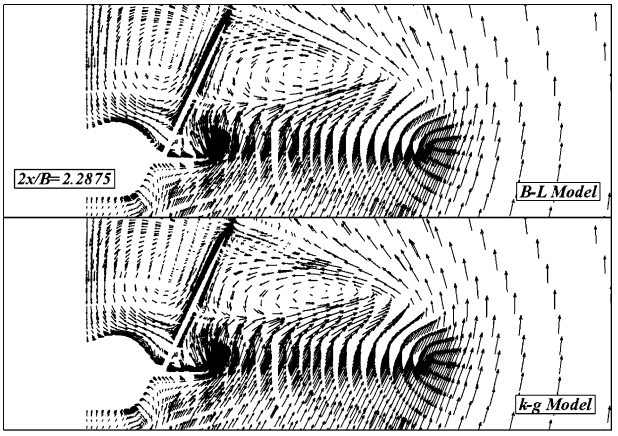

Fig. 9d Velocity vectors at $2x/B = 2.2875$, AOA = 24 deg.

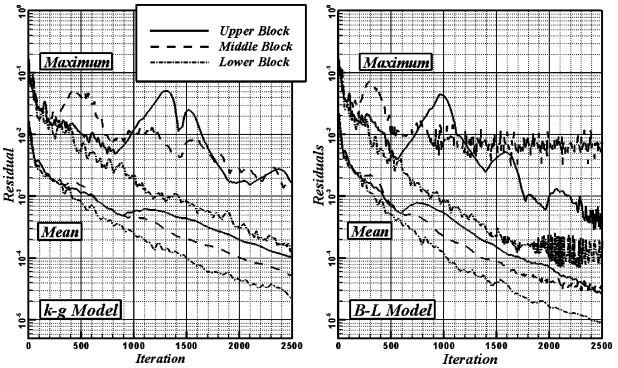

Fig. 9e History of maximum and mean residuals, AOA = 24 deg.

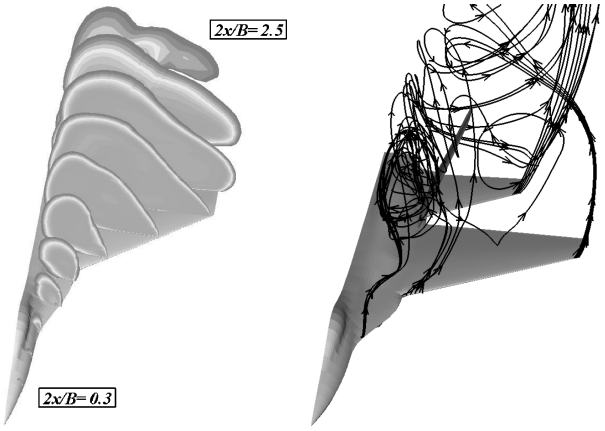

Fig. 10a Vortices over the upper surface, AOA = 40 deg.

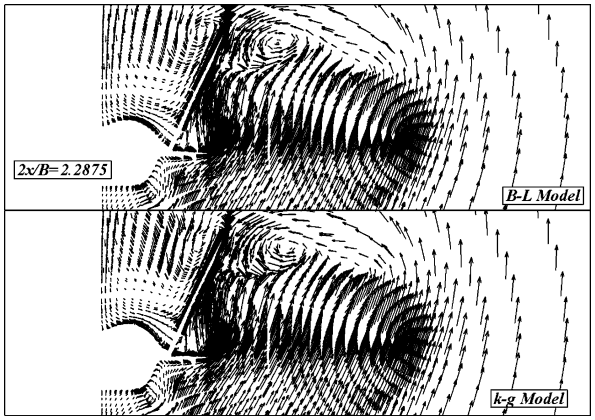

Fig. 10b Velocity vectors at $2x/B = 2.2875$, AOA = 40 deg.

effect of high AOA flow, the residual of the steady computation is hard to decrease in some places. However, the total force and moment results are all iterated to an approximately steady state in our computation.

Case 3: AOA = 40 Degrees

It is still very difficult for transonic wind-tunnel experiments to test accurately the complete aircraft configuration at very high AOA (here > 24). In the k–g results shown in Fig. 10a (AOA $= 40$ deg), the vortex from the strake becomes much stronger. The vertical tail is completely submerged in the vortices from the strake, the wing, and even the forebody. A change of the flow structure is also observed within the passage between the vertical tail and fuselage in Fig. 10a, where the vortex core is abruptly enlarged. This indicates that the strake vortex has undergone a breakdown. As shown in Fig. 10a, the breakdown seems to be a bubble type.

The velocity vectors at station $2x/B = 2.2875$ are shown in Fig. 10b. The cores of vortices move upward more obviously than in both cases 1 and 2, whereas the tendency of outward movement is weakened. The interaction between the vortex structure and the vertical tail becomes very severe.

V. Conclusions

The k–g model is capable of being applied in transonic high-AOA flow about complex configurations. The results demonstrated its superiority when compared to the B–L model and the k–ω model. Furthermore, it is very easy to realize and demonstrates very good numerical properties in computation, which makes it very attractive to CFD researchers in engineering fields.

However, being not a widely used model yet, the k–g model needs to be much more comprehensively understood in the future work. More impertantly, the mechanisms of the limiter R need to be well studied.

Acknowledgments

The first author got his Ph.D. from Northwestern Polytechical University in 2003. The author gratefully acknowledges his research group in NWPU, specifically Qin E., Jie Li, and Weimin Sang and the rest of the team.

References

[1]Kandula, M., and Wilcox, D. C., "An Examination of k–ω Turbulence Model for Boundary Layers, Free Shear Layers and Separated Flows," AIAA Paper 95-2317, June 1995.

[2]Wilcox, D. C., "Reassessment of the Scale-Determining Equation for Advanced Turbulence Models," *AIAA Journal*, Vol. 26, No. 11, 1988, pp. 1299–1310.

[3]Menter, F. R., "Two-Equation Eddy-Viscosity Turbulence Models for Engineering Applications," *AIAA Journal*, Vol. 32, No. 8, 1994, pp. 1598–1605.

[4]Kalitzin, G., Gould, A. R. B., and Benton, J. J., "Application of Two-Equation Turbulence Models in Aircraft Design," AIAA Paper 96-0327, Jan. 1996.

[5]Runckel, J. F., and Lee, E. E., Jr., "Investigation at Transonic Speeds of the Loading over a 45 deg Sweptback Wing Having an Aspect Ratio of 3, a Taper Ratio of 0.2, and NACA 65A004 Airfoil Sections," NASA TN D-712, May 1961.

[6]Fengwei, L., Qin, E., Jie, L., Guowei, Y., and Haixin, C., "The Strategy on Grids Generation for Real Aircraft and Application in CFD for Aviation," *First Numeric Grids Generation Methods Conference*, Aug. 1997.

[7]Bladwin, B., and Lomax, H., "Thin-Layer Approximation and Algebraic Model for Separation Flows," AIAA Paper 78-257, Jan. 1978.

[8]Wilcox, D. C., *Turbulence Modeling for CFD*, 2nd edition, DCW Industries, Inc., La Canada, CA, 1998, Chap. 4.

[9]Menter, F. R., "Zonal Two Equation k–ω Turbulence Models for Aerodynamic Flows," AIAA Paper 93-2906, July 1993.

[10]Johnson, D. A., and King, L. S., "A Mathematical Simple Turbulence Closure Model for Attached and Separated Turbulent Boundary Layers," *AIAA Journal*, Vol. 23, No. 11, 1985, pp. 1684–1692.

[11]Jameson, A., Schmidt, W., and Turkel, E., "Numerical Solutions of Euler Equations by Finite Volume Methods with Runge–Kutta Time Stepping Schemes," AIAA Paper 81-1259, June 1981.

[12]Swanson, R. C., and Turkel, E., "Artificial Dissipation and Central Difference Schemes for Euler and N–S Equations," AIAA Paper 87-1107, June 1987.

[13]Swanson, R. C., and Turkel, E., "On Central-Difference and Upwind Schemes," *Journal of Computational Physics*, Vol. 101, No. 2, 1992, pp. 292–306.

[14]Couaillier, V., "Numerical Simulation of Separated Turbulent Flows Based on the Solution of RANS/Low Reynolds Two-Equation Model," AIAA Paper 99-0154, Jan. 1999.

[15]Zhixiang, X., Jie, L., Fengwei, L., and Chuanjing, L., "Application of Turbulence Models in Simulation of Complex Flow-Fields," AIAA Paper 2003-3745, June 2003.